Earth and Planetary Science Letters 503 (2018) 108–117

Contents lists available at ScienceDirect

Earth and Planetary Science Letters

www.elsevier.com/locate/epsl

# Absence of thermal influence from the African Superswell and cratonic keels on the mantle transition zone beneath southern Africa: Evidence from receiver function imaging

Muchen Sun [a,b], Xiaofei Fu [a], Kelly H. Liu [b], Stephen S. Gao [b,*]

[a] College of Earth Science and Research Institute of Unconventional Oil and Gas, Northeast Petroleum University, Daqing, Heilongjiang 163318, China
[b] Geology and Geophysics Program, Missouri University of Science and Technology, Rolla, MO 65409, USA

ARTICLE INFO

*Article history:*
Received 8 May 2018
Received in revised form 4 September 2018
Accepted 11 September 2018
Available online 3 October 2018
Editor: R. Bendick

*Keywords:*
mantle transition zone
Southern Africa
African Superswell
receiver function
Lithosphere

ABSTRACT

The depths of the 410 km (*d*410) and 660 km (*d*660) discontinuities beneath southern Africa, which is presumably underlain by the lower-mantle African Superswell, are imaged in 1° radius consecutive circular bins using over 6400 *P*-to-*S* receiver functions (RFs) recorded by 130 seismic stations over a 27 yr period. When the IASP91 standard Earth model is utilized for moveout correction and time-depth conversion, a normal mantle transition zone (MTZ) thickness of 246 ± 7 km is observed, suggesting that the Superswell has no discernible effect on mantle transition zone temperature. Based on the negligible disparity of the mean MTZ thicknesses between on (246 ± 6 km) and off (246 ± 8 km) cratonic regions, we conclude that the deep Archean cratonic keels possess limited influence on MTZ thermal structure. The apparently shallower-than-normal MTZ discontinuities and the parallelism between the *d*410 and *d*660 are mostly the results of upper mantle high wave speed anomalies probably corresponding to a thick lithosphere with a mean thickness of about 245 km beneath the Kaapvaal and 215 km beneath the Zimbabwe cratons. In contradiction to conclusions from some of the previous studies, the resulting spatial distribution of the stacking amplitudes of the *P*-to-*S* converted phases at the discontinuities is inconsistent with the presence of an excessive amount of water in the MTZ and atop the *d*410.


## 1. Introduction

In spite of numerous observational and geodynamic modeling studies, mechanisms responsible for the anomalously high topography of southern Africa (Fig. 1) remain controversial (Lithgow-Bertelloni and Silver, 1998; Hu et al., 2018). One of the most commonly invoked hypotheses is the dynamic effects of the African Superswell, a low-seismic wave speed anomaly in the lower mantle beneath most of the southern hemispheric region of Africa and the neighboring oceanic areas of the African Plate (Lithgow-Bertelloni and Silver, 1998; Romanowicz and Gung, 2002; Ni et al., 2005). Whether the presumably high temperature from the Superswell has influenced the structure and deformation (especially rifting) of the upper mantle and mantle transition zone (MTZ), a layer of the Earth sandwiched between the 410 km (*d*410) and 660 km (*d*660) discontinuities, is still a debated subject (Ritsema et al., 1998; Priestley et al., 2008; Fishwick, 2010; Youssof et al., 2015). Another controversial issue is the depth extent of the cratonic keels and their influence on the temperature distribution in the upper mantle and MTZ. Beneath the Kaapvaal and Zimbabwe cratons, seismic surface wave studies suggested a lithospheric thickness of 160–250 km (Li and Burke, 2006; Chevrot and Zhao, 2007; Priestley et al., 2008; Schaeffer and Lebedev, 2013), while other studies especially those using teleseismic body-waves (James et al., 2001; Youssof et al., 2015) revealed a much thicker lithosphere, down to about 300 to 350 km, which may cause low temperature anomalies in the MTZ (Blum and Shen, 2004). The discrepancy is most likely caused by the limited resolving power and the consequent large uncertainties in the tomographic methods. Body-wave tomographic techniques pervasively utilize relative (rather than absolute) travel time residuals and thus the resulting wave speed anomalies are relative to the mean over the region investigated (Foulger et al., 2013). Additionally, they suffer from vertical smearing due to the steep ray paths beneath the station. In contrast, surface-wave tomographic techniques produce absolute wave speed anomalies, and have inherently better vertical resolution but poorer horizontal resolution due to lateral smearing.

* Corresponding author.
*E-mail address:* sgao@mst.edu (S.S. Gao).

https://doi.org/10.1016/j.epsl.2018.09.012
0012-821X/

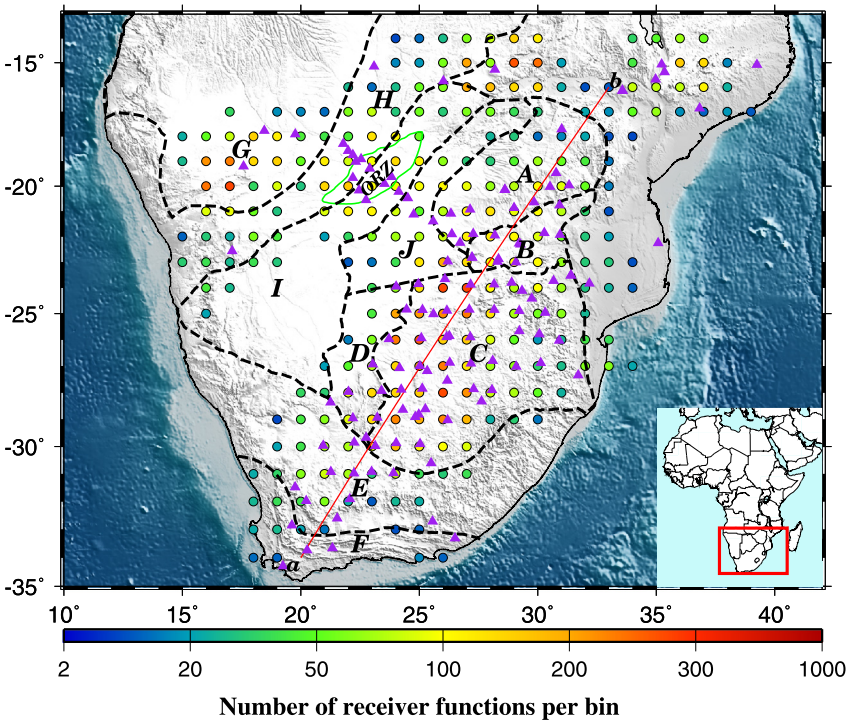


**Fig. 1.** Topographic relief map of the study area showing the center of radius = 1° bins (filled circles), and major tectonic boundaries (black dashed lines). The color of the circles represents the number of the RFs per bin. The purple triangles are seismic stations used in the study. The subareas include: A: Zimbabwe Craton; B: Limpopo Belt; C: Kaapvaal Craton; D: Kheiss Belt; E: Namaqua–Natal Belt; F: Cape Fold Belt; G: southern Congo Craton; H: Damara Belt; I: Rehoboth Province; J: Magondi Belt. Line a–b indicates the location of the profile shown in Fig. 8. The red rectangle in the inset map shows the study area. (For interpretation of the colors in the figure(s), the reader is referred to the web version of this article.)

It has long been recognized that the topography of the *d*410 and *d*660 can provide independent constraints on the thermal and wave speed structures of the upper mantle and MTZ (Anderson, 1967; Flanagan and Shearer, 1998). The discontinuities reflect sudden changes in mineralogical phases, from olivine to wadsleyite at the *d*410, and from ringwoodite to bridgmanite at the *d*660 (Ringwood, 1975). Due to the opposite sign of the Clapeyron slopes (ranging from +1.5 MPa/K to +4.0 MPa/K for *d*410 and from −0.2 MPa/K to −4.0 MPa/K for *d*660; Tauzin and Ricard, 2014), high and low temperature anomalies can result in a thinner-than-normal and thicker-than-normal MTZ, respectively. In addition, the existence of water-saturated minerals in the MTZ could thicken the MTZ (Litasov et al., 2005), and an excessive amount of water tends to broaden the interval of the olivine–wadsleyite phase transition and reduce the sharpness of the *d*410 (Wood et al., 1996; Smyth and Frost, 2002; van der Meijde et al., 2003). Therefore, variations of the depths and sharpness of the *d*410 and *d*660 are effective indicators of spatial variations of thermal perturbations and water content anomalies in the vicinity of the MTZ discontinuities (Ringwood, 1975).

Several MTZ studies have been conducted in southern Africa with controversial conclusions. Gao et al. (2002) estimated an MTZ thickness of 245 km that is comparable to the global average, and suggested that the lower-mantle African Superswell beneath southern Africa has no observable influence on the MTZ temperature. In contrast, Blum and Shen (2004) detected a 20 km thicker-than-normal MTZ beneath the Archean cratons in southern Africa, and interpreted it as the consequence of the extension of low-temperature, water-saturated Archean cratonic keels to the base of the MTZ. Another MTZ study (Niu et al., 2004) showed a normal MTZ thickness and suggested that the highly depleted root causes an approximately 20 km apparent uplift of the *d*410 and *d*660 relative to the global average beneath the Kaapvaal craton. Julia and Nyblade (2013) utilized 2557 *P*-to-*S* receiver functions (RFs) from 30 permanent broadband stations in Africa, including 7 stations in our study area (Fig. 1), to image the MTZ discontinuities. They reported *d*410 depths in the range of 405 ± 10 km, and *d*660 depths of 655 ± 11 km with a mean MTZ thickness of 250 ± 3 km beneath southern Africa. A recent MTZ study across the Okavango Rift zone conducted by Yu et al. (2015) revealed apparently shallower-than-normal MTZ discontinuities beneath the northern Kalahari Craton and a normal MTZ thickness beneath most of the study area, suggesting the absence of mantle plumes beneath the incipient rift.

The discrepancies in the results and conclusions from previous MTZ studies in southern Africa (Gao et al., 2002; Shen and Blum, 2003; Blum and Shen, 2004; Niu et al., 2004) are mostly the results of the limited amount of seismic data and the different methodologies applied by different research groups. In this study, we apply a non-plane wave assumption approach (Gao and Liu, 2014a) to an expanded data set recorded over the past 27 yr to provide an enhanced image of the MTZ discontinuities beneath southern Africa. Relative to methodologies based on the plane-wave assumption, our approach can lead to sharper MTZ discontinuity arrivals and more accurately determined depths (Gao and Liu, 2014a). In addition to the unprecedented number of high quality RFs used in this study, the spatial coverage is more extensive than the aforementioned regional-scale studies. The results provide tighter and more reliable constraints on the deep structure and temperature and water content of the upper mantle and MTZ beneath two of the oldest cratons on Earth, and the only continental area that is presumably underlain by a lower-mantle superswell.

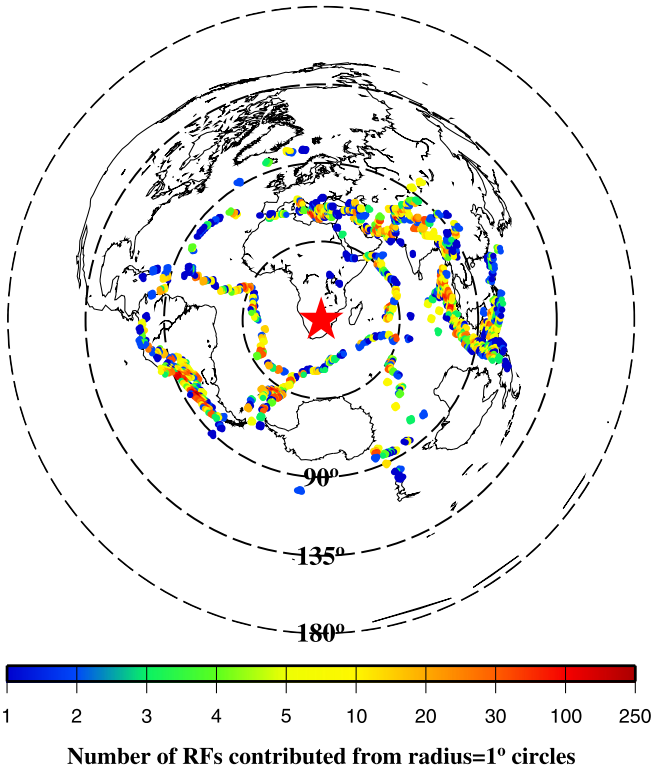


**Fig. 2.** Spatial distribution of earthquake source areas. Each dot represents a radius = 1° circular area. The distance between neighboring circles is 1°. The color of the dot represents the number of used RFs originated from earthquakes in the circle. The radius of the concentric dashed circles centered at the central part of the study area (star) indicates the epicentral distance.

## 2. Data and methods

### 2.1. Data

All the available teleseismic data recorded by three-component broad-band stations located in the study area (14°S to 35°S, and 15°E to 40°E) during the period between 1990 and 2017 were requested from the Incorporated Research Institutions for Seismology (IRIS) Data Management Center (DMC). The cut-off magnitude ($M_c$) for requesting data is determined based on the empirical equation to balance the quality and quantity of the data to be requested, i.e., $M_c = 5.2 + (\Delta - 30.0)/(180.0 - 30.0) - D/700.0$, where $\Delta$ and $D$ are the epicentral distance (ranging from 30° to 100°) in degrees and focal depth in kilometers, respectively (Liu and Gao, 2010). The requested three-component seismograms with a length of 280 s, including 20 s before and 260 s after the theoretical arrival of the first compressional wave calculated based on the IASP91 Earth model, were filtered in the frequency band of 0.02–0.2 Hz. Vertical-component seismograms were assessed for signal-to-noise ratio (SNR) using the method of Gao and Liu (2014a). If the SNR exceeded 4.0, the filtered 3-component seismograms were converted into radial RF following the procedure of Ammon (1991). Then the receiver functions were checked visually to reject the ones without a clear first $P$ pulse, or those with abnormal arrivals that are stronger than the first $P$ pulse. Among the 6907 three-component seismograms with a SNR greater than 4.0, a total of 6472 high-quality RFs recorded by 130 stations from 1302 events (Fig. 2) were used in this study. In comparison, the number of RFs used by Gao et al. (2002) and Blum and Shen (2004) in the similar study area is 1300 and 3354, respectively.

### 2.2. Moveout correction and stacking

The data processing steps and parameters used in this study are discussed in detail in Gao and Liu (2014b), and are briefly summarized here. The RFs are grouped into 1° radius circular bins based on the locations of ray-piercing points computed at the middle of the MTZ (535 km depth) according to the IASP91 Earth model. The bin size is approximately comparable to that of the first Fresnel zone of shear waves at the MTZ depths. Comparing with the traditional common conversion point stacking approach of grouping the RFs for each depth of assumed discontinuities (e.g., Dueker and Sheehan, 1998; Liu et al., 2003), this approach ensures that both MTZ discontinuities are sampled by the same RFs, minimizing possible biases on the resulting MTZ thickness by upper mantle wave speed heterogeneities (Gao and Liu, 2014b; Dahm et al., 2017).

RFs in each of the bins are moveout corrected and stacked using a non-plane wave assumption approach (Gao and Liu, 2014a) to form a depth series in the depth range of 300–800 km with a vertical grid size of 1 km under the 1-D IASP91 Earth model. Relative to approaches assuming a plane wavefront, the non-plane wave assumption approach can more accurately determine the discontinuity depths and result in sharper discontinuity images due to the consideration of the difference in ray parameters between the direct $P$-wave and the converted $S$-wave. Only the results from bins with 10 or more RFs are used for the study. The optimal depth of the $d410$ corresponds to that of the maximum stacking amplitude in the depth range of 380–440 km, and that of the $d660$ corresponds to the depth of the largest arrival in the range of 630–690 km. For a small fraction (about 5%) of the bins, multiple arrivals with comparable amplitudes are present in the search window. For these bins, the search ranges are manually adjusted to maintain spatial continuity. The mean and standard deviation of the MTZ discontinuity depths and MTZ thickness for each bin are obtained following a bootstrap resampling procedure with 50 resampling iterations (Efron and Tibshirani, 1986).

### 2.3. Wave speed correction

Since the 1-D IASP91 standard Earth model is utilized to moveout-correct the RFs, the resulting MTZ discontinuity depths are apparent instead of true depths, which can be obtained if $P$- and $S$-wave speed models extending through the crust, upper mantle and MTZ are available in digital form. If only the $V_p$ ($V_s$) model is available, a $\gamma$ factor, which is defined as $d\ln(V_s)/d\ln(V_p)$, is assumed or searched (e.g., Gao and Liu, 2014b) to generate the $V_s$ ($V_p$) model.

In this study, two wave speed models (Schaeffer and Lebedev, 2013 and updated in 04/2018; Youssof et al., 2015), which include both $V_p$ and $V_s$ anomalies in digital forms, are used to conduct the wave speed corrections by following the procedure of Gao and Liu (2014b) for correcting the MTZ discontinuity depths beneath the contiguous United States. To perform the correction, the wave speed anomalies are smoothed using the cubic B-spline function, and the average $P$- and $S$-wave speeds are calculated in radius = 1° cylinders with a 10 km thickness for the depth range of 0–700 km. Lastly, the equation (Gao and Liu, 2014b)

$$H_T = \frac{(V_{s0} + \delta V_s) \times (V_{p0} + \delta V_p)}{V_{p0} + \delta V_p - V_{s0} - \delta V_s} \times \frac{V_{p0} - V_{s0}}{V_{p0} \times V_{s0}} H_A \quad (1)$$

is applied to convert the apparent depths ($H_A$) into true depths ($H_T$), where $V_{p0}$ and $V_{s0}$ are the mean $P$- and $S$-wave speeds in the layer in the standard Earth model, and $\delta V_p$ and $\delta V_s$ are the absolute $P$- and $S$-wave speed anomalies.

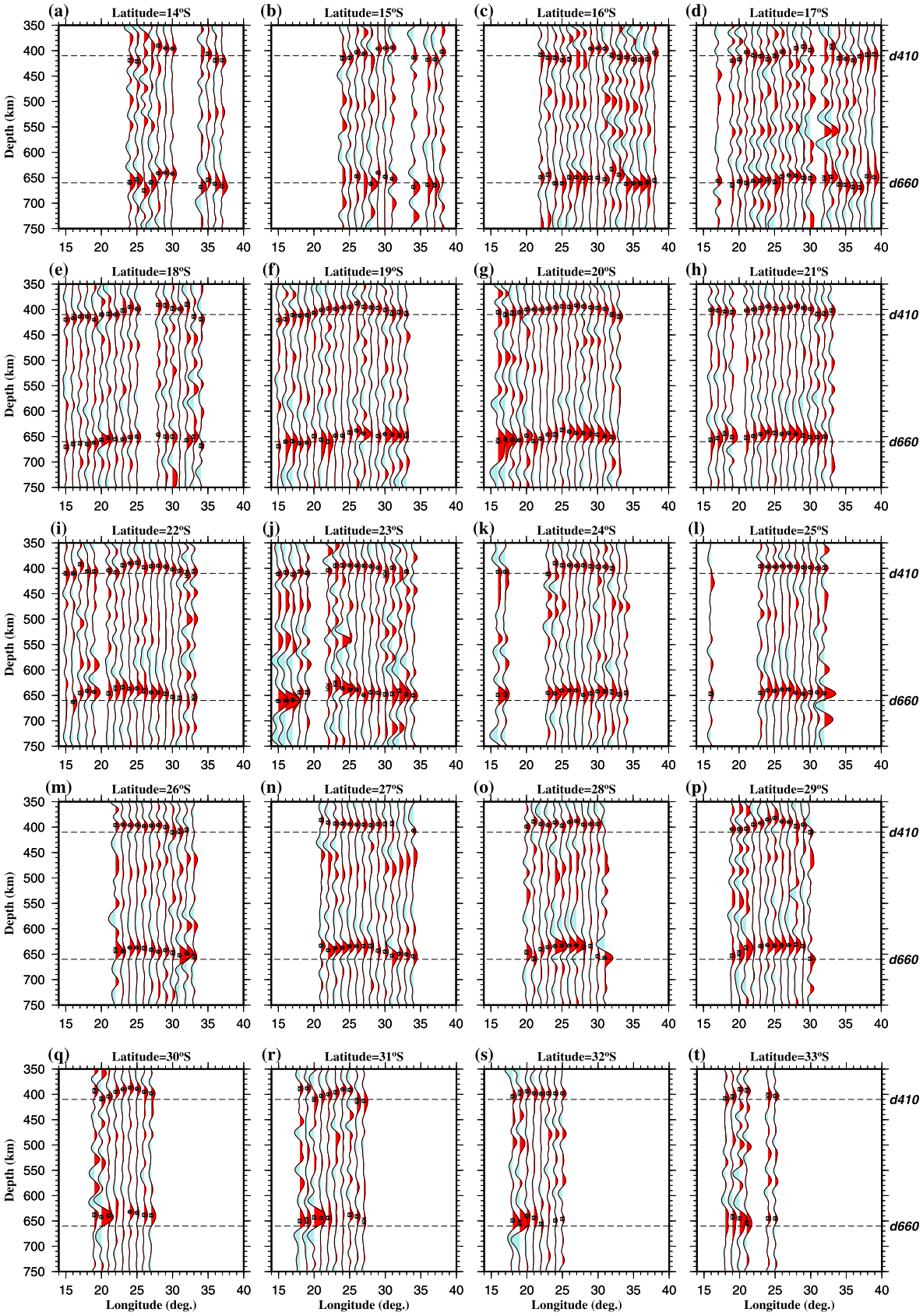


**Fig. 3.** Results of stacking moveout-corrected RFs within each bin plotted along 20 latitudinal profiles. The black traces show the depth series averaged over all the 50 bootstrap iterations. The circles and error bars respectively represent the resulting apparent depths and standard deviations of the depths of the MTZ discontinuities.

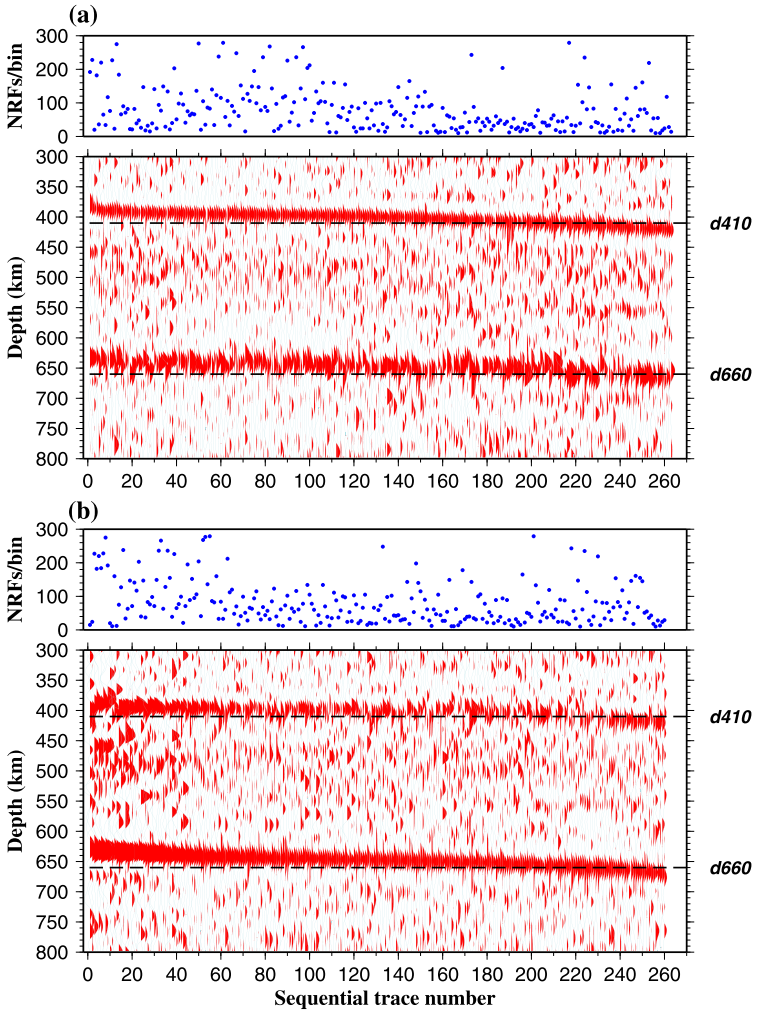


**Fig. 4.** (a) Results of stacking all available normal moveout corrected RFs from 1° radius bins with a minimum of 10 high-quality RFs, plotted against the sequentially increasing depth of the *d*410. (b) Similar to (a) but against the sequentially increasing depth of the *d*660. The top panel in (a) and (b) shows the number of RFs per bin.

## 3. Results

All the 20 latitudinal profiles (from 14°S to 33°S) of the resulting depth series in the study area are shown in Fig. 3. Robust peaks for the *d*410 or *d*660 are observed in a total of 281 bins (Fig. 4), among which 263, 260, and 242 possess reliable arrivals from the *d*410, *d*660, and both, respectively.

### 3.1. Apparent discontinuity depths and MTZ thickness

The resulting apparent *d*410 and *d*660 depths (Figs. 5a and 5b; Table S1) show systematic spatial variations and are positively correlated with a cross correlation coefficient (XCC) of 0.7 (Fig. 6). On average, the Kaapvaal and Zimbabwe cratons show a 10–15 km (Fig. 5 and Table S2) apparent uplift of both MTZ discontinuities with a maximum value of about 30 km, while the surrounding Proterozoic fold belts demonstrate normal discontinuity depths. For the entire study area, the mean apparent depths are 401 ± 9 km and 648 ± 9 km for the *d*410 and *d*660, respectively. The corresponding values are 395 ± 5 km and 640 ± 7 km for the Kaapvaal Craton, and 398 ± 5 km and 647 ± 4 km for the Zimbabwe Craton (Table S2). The boundary of the area with apparently shallower MTZ discontinuities follows the surface expression of the Kaapvaal Craton well, but shifts to the west by about 200 km from the western boundary of the surface expression of the Zimbabwe Craton (Fig. 5). In spite of the obvious difference in the apparent *d*410 and *d*660 depths between on and off cratonic regions (Table S2), a negligible disparity of the mean MTZ thickness between on (246 ± 6 km) and off (246 ± 8 km) cratonic regions is observed in the study area (Fig. 5c).

The average MTZ thickness is 246 ± 7 km (Fig. 5c), which is statistically identical to the global average (which ranges from 240 to 250 km) reported by previous global scale studies (Flanagan and Shearer, 1998; Gu et al., 1998; Tauzin et al., 2008). The depths and thickness measurements are generally consistent with most of the previous MTZ studies targeting the Kaapvaal and Zimbabwe cratons (Gao et al., 2002; Niu et al., 2004; Julia and Nyblade, 2013) and the Okavango Rift zone (Yu et al., 2015). They are also in agreement with results from several stations in southern Africa from global scale studies (Flanagan and Shearer, 1998; Chevrot et al., 1999; Tauzin et al., 2008), but are inconsistent with the results of Shen and Blum (2003) and Blum and Shen (2004) who reported a 20 km thicker-than-normal MTZ beneath the Archean cratons in southern Africa due to shallowing of the *d*410 and deepening of the *d*660, and interpreted it as the consequence of lowered temperature originating from the cold deep cratonic keels.

### 3.2. Spatial variation of stacking amplitudes

We use the ratio ($R$) between the amplitude of the $P$-to-$S$ converted phase ($Pds$) from an MTZ discontinuity and that of the

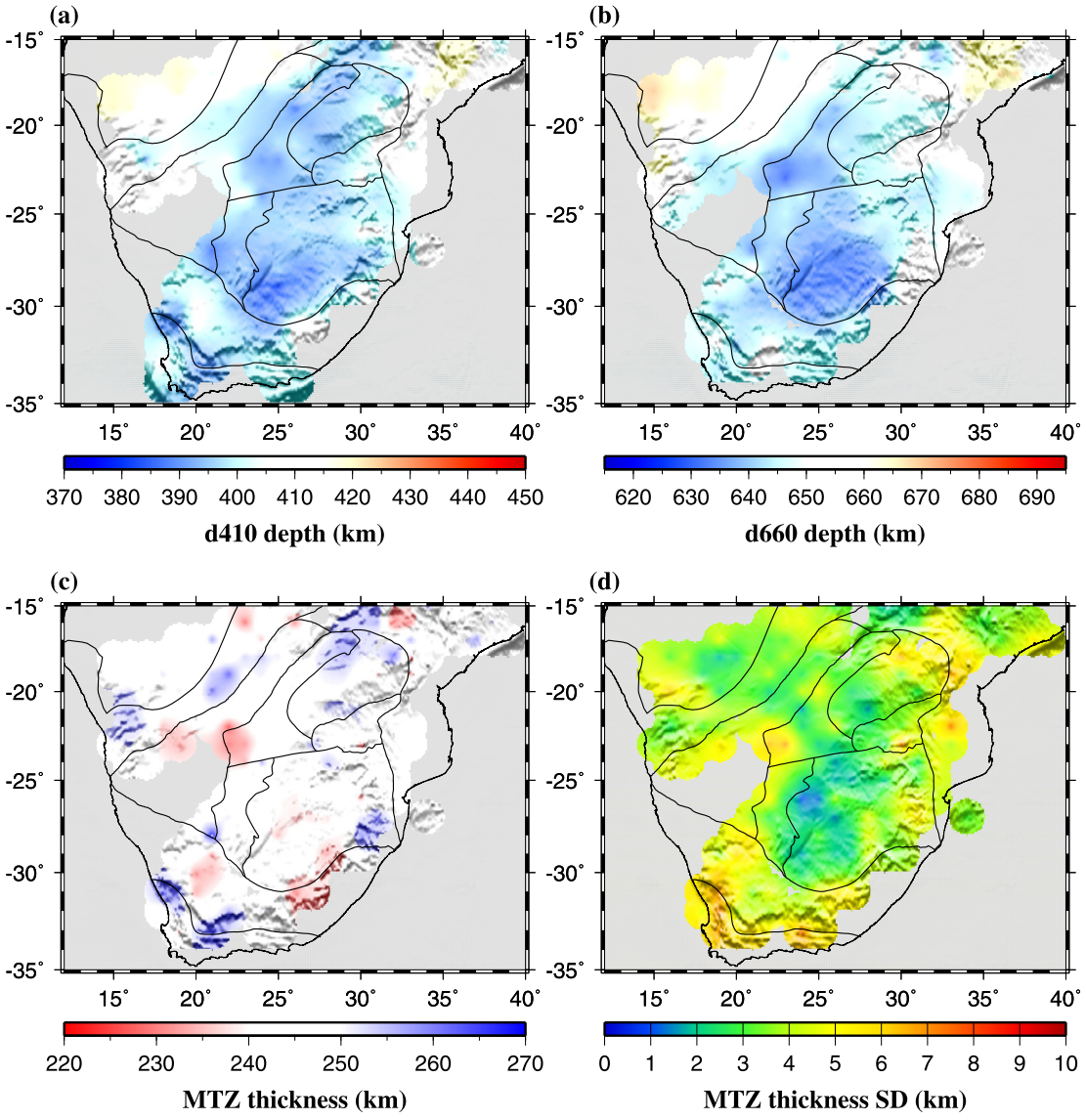


**Fig. 5.** (a) Spatial distribution of resulting *d*410 depths. (b) Same as (a) but for the *d*660. (c) MTZ thickness measurements. (d) Standard deviation (SD) of the MTZ thickness measurements.

direct *P*-wave as a measure of the wave speed contrast across, and the sharpness of, the discontinuity (Fig. 7). For the entire study area, the average *R* value is 0.021 ± 0.008 for the *d*410 and 0.023 ± 0.007 for the *d*660, both are greater than that beneath tectonically stable central North America (0.018 ± 0.005 for the *d*410 and 0.019 ± 0.004 for the *d*660), and active western North America (0.015 ± 0.005 for the *d*410 and 0.016 ± 0.004 for the *d*660) (Gao and Liu, 2014b). The stronger stacking amplitudes of the *Pds* observed beneath southern Africa might indicate the existence of a less attenuative upper mantle relative to western and central North America. Under this assumption, the absence of a clear correspondence between the *R* observations and the tectonic provinces (Fig. 7) may suggest that there is no obvious age dependence of upper mantle attenuation.

### 3.3. Wave speed corrected depths

The *P*- and *S*-wave speed models of Schaeffer and Lebedev (2013) and Youssof et al. (2015), which cover the entire and most of the study area, respectively, are utilized for wave speed corrections in this study. As detailed in Gao and Liu (2014b), the accuracy of the wave speed correction can be estimated using the degree of reduction in the XCC between the corrected depths of *d*410 and *d*660. This is primarily because of the fact that wave speed anomalies in the upper mantle (above the *d*410) lead to positive correlations between the apparent depths of the two discontinuities (Fig. 6), while thermally or water content induced wave speed anomalies in the MTZ normally result in negative correlations between the true depths of the two discontinuities. Therefore, if the wave speed anomalies used for the correction are precisely determined, the resulting XCC should reduce to zero if there is no thermal, water content, or other anomalies that affect the depths of the discontinuities; the XCC becomes a negative value if thermal or water content anomalies exist in the MTZ.

The corrected depths and MTZ thickness as well as the resultant XCC values are shown in Figs. S1 and S2. Although the correction by using the models of Schaeffer and Lebedev (2013) reduces the XCC from 0.7 before the correction to 0.58 afterward, the corrected *d*410 and *d*660 depths are still positively correlated. The XCC between the corrected depths by using the models of Youssof et al. (2015) only reduces marginally, from 0.70 to 0.67, indicating that the wave speed corrections did not effectively remove the influence of upper mantle wave speed anomalies on the apparent

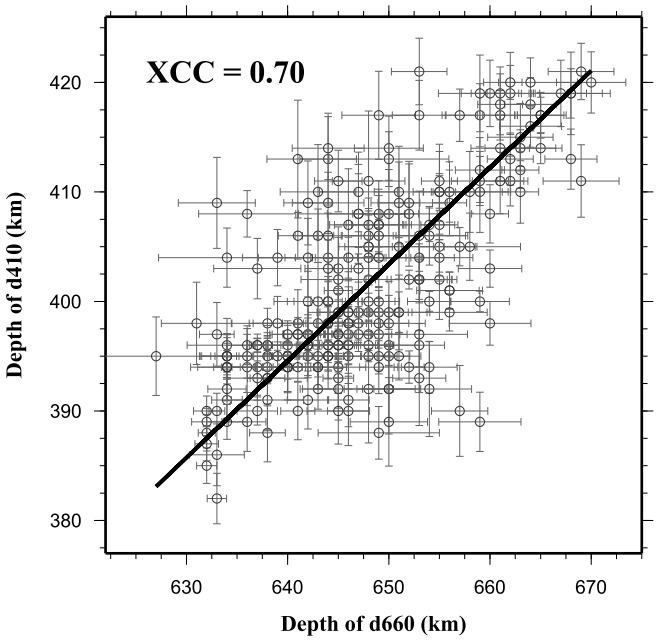


**Fig. 6.** Correlation plot of apparent $d410$ and $d660$ depths. The line indicates the optimal bivariate regression with a cross-correlation coefficient of 0.70.

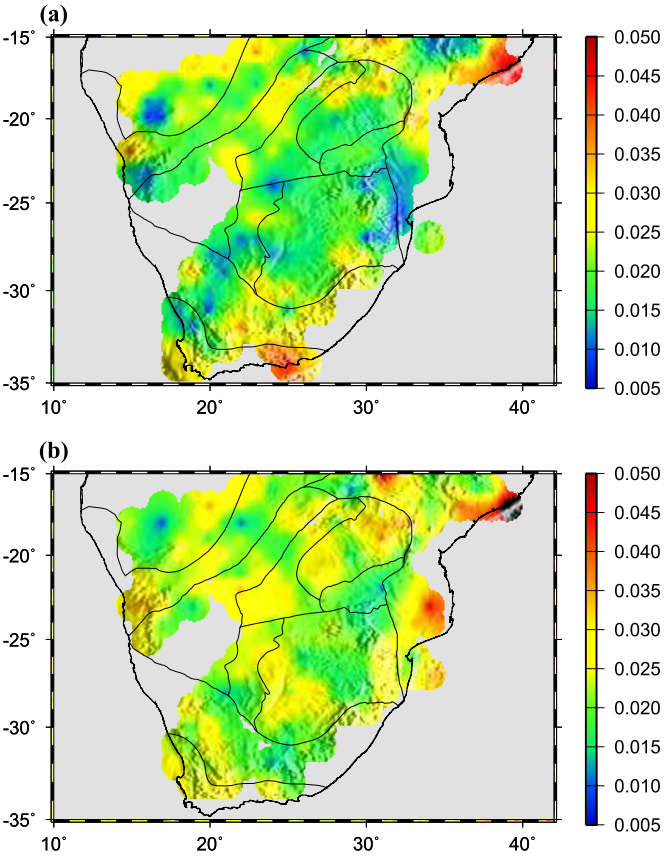


**Fig. 7.** Stacking amplitude (relative to that of the direct $P$-wave) for (a) $d410$ and (b) $d660$.

depths. In comparison, the XCC reduced from 0.84 to 0.41 after the same wave speed correction procedure was applied for the contiguous United States (Gao and Liu, 2014b). We also tried a few other wave speed models (e.g., Priestley et al., 2008) with available $V_p$ and/or $V_s$ anomalies in digital form, and found that none of them was able to significantly reduce the XCC.

The small reduction in the XCCs between the corrected $d410$ and $d660$ depths suggests that the wave speed corrected depths are not reliable, most likely due to large uncertainties in the models and under-estimation of the amplitude of the wave speed anomalies. Additionally, considerable discrepancies are present among existing wave speed models (e.g., Fig. S3) and thus it is difficult to determine which of the wave speed corrected results is the most realistic one. Therefore, in the following we discuss the wave speed structure in the upper mantle and the thermal and water content anomalies in the vicinity of the MTZ discontinuities using the apparent (Fig. 5) rather than the wave speed corrected (Figs. S1 and S2) depths.

## 4. Discussion

### 4.1. Thermal structure of the MTZ

The simplest explanation for the observed nearly normal MTZ thickness beneath most of southern Africa (Fig. 5c) is that there is no discernible temperature anomaly in the MTZ. However, some specific combinations of temperature and water content anomalies may lead to a normal MTZ thickness (Reed et al., 2016; Sun et al., 2017). The first scenario is when the effect of water (which can uplift the $d410$ and depress the $d660$; Litasov et al., 2005) and that of higher-than-normal temperature (which has an opposite effect than water on the discontinuities) coincidentally cancel each other, leading to a normal MTZ thickness. However, these two factors are unlikely to cancel each other almost everywhere across this study area with a diverse set of tectonic provinces and lithospheric ages and thicknesses (Fig. 1). In addition, the lack of an anomalously high amount of water in the MTZ is consistent with the observation that a low wave speed layer is not observed atop the $d410$ beneath southern Africa (Tauzin et al., 2010), a conclusion that is supported by the stacked RFs from this study (Figs. 3 and 8).

The second scenario to produce a normal MTZ thickness is when the amount of uplift of the $d660$ caused by the higher-than-normal temperature from the lower mantle superswell matches that of the $d410$ caused by the lower-than-normal temperature from the deep cratonic keels. However, because the superswell covers a much larger area than the cratons (Ritsema et al., 1999), thinner-than-normal MTZ thickness should be expected beneath the off cratonic areas due to the absence of the effect of the keels. This prediction is inconsistent with the observed MTZ thicknesses, which are similar between cratonic ($246 \pm 6$ km) and off cratonic ($246 \pm 8$ km) areas (Fig. 5c and Fig. 8).

Therefore, we conclude that the presence of an excessive amount of water or significant thermal anomalies in the MTZ is unlikely. This in turn suggests that neither the lower-mantle African Superswell nor the cratonic keels have a discernible effect on the MTZ temperature. The conclusion that the thermal influence of the cratonic keels is limited to the upper mantle and does not extend to the MTZ is consistent with most previous tomographic studies (James et al., 2001; Wittlinger and Farra, 2007; Priestley et al., 2008; Fishwick, 2010; Youssof et al., 2015). Similarly, the observed dominantly normal MTZ thickness beneath cratonic areas in North America indicates the absence of significant influence of cratonic keels on the thermal structure of the MTZ (Thompson et al., 2011; Gao and Liu, 2014a).

### 4.2. Upper mantle wave speed anomalies derived from the apparent discontinuity depths

As discussed in the previous section, large scale significant thermal and water content anomalies are unlikely to exist in the

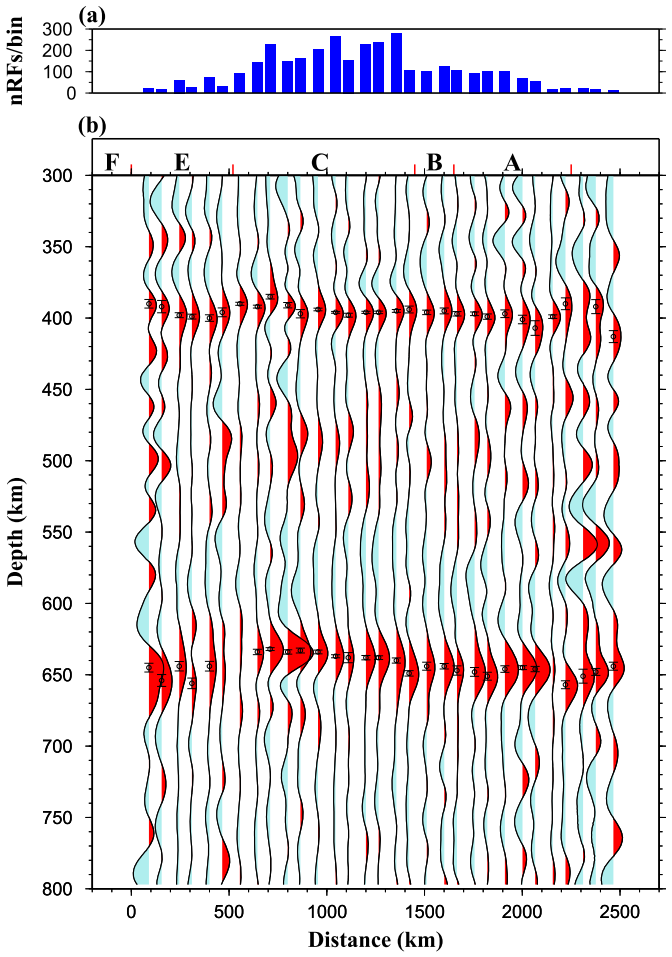


**Fig. 8.** (a) Number of RFs in bins within a 150 km wide band centered at Profile a–b shown in Fig. 1. (b) Resulting depth series in the bins. The letters at the top indicate the five subareas in Fig. 1.

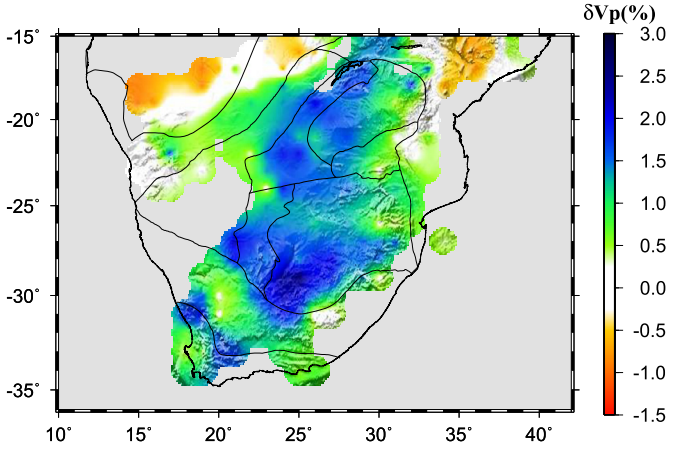


**Fig. 9.** Required $P$-wave velocity anomalies (relative to the IASP91 Earth model) in order to correct the observed apparent $d410$ depths to a uniform true depth of 410 km.

MTZ beneath southern Africa. In addition, the parallelism between the shallower-than-normal apparent depths of the $d410$ and $d660$ (Fig. 5) suggests that high wave speed anomalies situated above the $d410$ are the simplest explanation for the apparent uplift of both discontinuities. Under the assumption that the true depth of the $d410$ is 410 km, the apparent depth of the $d410$ can be used to estimate the mean upper mantle $P$- and $S$-wave speed anomalies for an assumed $\gamma$ factor (Gao and Liu, 2014b). For the following calculations, we assume that $\gamma = 1.7$, a value that was estimated for the central and eastern United States (Gao and Liu, 2014b). Application of a different factor would change the absolute wave speed anomalies, but not their spatial variations (Reed et al., 2016).

The resulting average upper mantle $P$-wave speed anomalies calculated using the relationship between the apparent depths of the MTZ discontinuities and wave speed anomalies (Equation (1)) correspond well with major tectonic boundaries (Fig. 9). The mean upper mantle $P$-wave speed anomaly required to correct the observed average apparent $d410$ depth (401 ± 8 km) to the depth of 410 km is 0.84 ± 0.84% for the entire study area, and 1.49 ± 0.49%, 1.20 ± 0.49%, and 0.83 ± 0.56% for the Kaapvaal Craton, Zimbabwe Craton, and Limpopo Belt, respectively.

While the spatial variations of the derived wave speed anomalies (Fig. 9) are in general agreement with those from most seismic tomographic results (James et al., 2001; Schaeffer and Lebedev, 2013; Fig. S3), the absolute amplitude of the variations obtained from this study is significantly greater than those from seismic tomographic investigations. Such a reduction in the amplitude in tomographically-derived wave speed models could be the result of a high damping factor that is necessary to stabilize the inversion, and for some previous studies, the use of relative rather than absolute travel time residuals (Foulger et al., 2013).

Under the assumption that the wave speed variations derived above are entirely caused by variations in lithospheric thickness, in the following we estimate the depth of the lithosphere–asthenosphere boundary (LAB) across the study area. To perform this task, a reference location on Earth with normal upper mantle wave speeds, a well imaged $d410$ with a nearly normal depth, and a reliably determined lithospheric thickness is needed. These conditions are satisfied by most parts of the eastern U.S., where normal apparent $d410$ depths and near zero average wave speed anomalies in the upper mantle (see Fig. 4a in Gao and Liu, 2014b) have been suggested. Additionally, for the easternmost U.S., the most recent $S$-to-$P$ receiver function study revealed a lithospheric thickness of ∼90 km (Liu and Gao, 2018), which is consistent with most of the previous studies (e.g., Rychert et al., 2007; Fischer et al., 2010).

Once the reference location with normal velocities and $d410$ depth is determined, the mean lithospheric thickness ($L$) beneath a given area with a mean relative upper mantle $V_p$ anomaly of $A$ (in percent) can be estimated by partitioning the anomaly from a layer with a thickness of 410 km to a layer of $(L - 90)$ km with a $V_p$ anomaly of $C$% determined in Section 4.2, i.e., $(L - 90)/A = 410/C + 90$, where 90 is the thickness of the lithosphere in km at the reference location. Obviously, for a fixed wave speed anomaly, a larger wave speed contrast requires a smaller difference in LAB depth relative to the reference location.

Fig. 10 shows the resulting mean lithospheric thickness plotted against assumed $C$ values beneath the Kaapvaal and Zimbabwe cratons and the Limpopo Belt, calculated based on the mean upper mantle $V_p$ anomalies shown in Table S2. If we assumed that the $V_p$ contrast between the lithosphere and the asthenosphere is 4%, a value suggested in numerous previous studies (e.g., Li et al., 2003; Rychert et al., 2007; Eaton et al., 2009; Yu et al., 2015), the lithospheric thickness would be about 245 km for the Kaapvaal Craton (Fig. 10). This value is generally consistent with most of the previous tomographic and receiver function studies (James et al., 2001; Niu et al., 2004; Wittlinger and Farra, 2007; Youssof et al., 2015). On the other hand, if the high wave speed root beneath the Kaapvaal Craton only extends to less than 200 km (Priestley et al., 2008; Fishwick, 2010), the required $V_p$ contrast between the lithosphere and asthenosphere would be greater than 5.6%, a high value that is not suggested by the existing studies for the area. The resulting lithospheric thick-

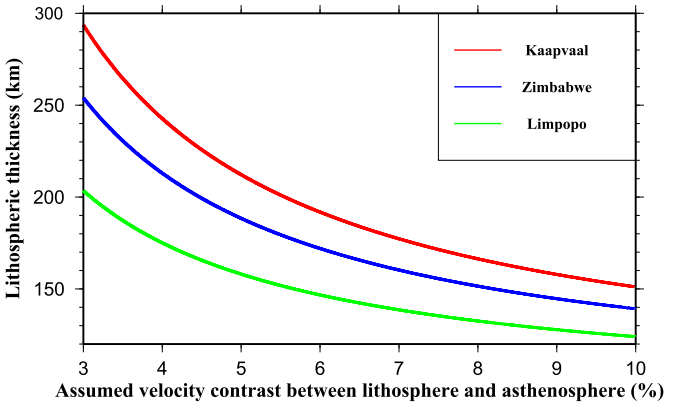


**Fig. 10.** Estimated lithospheric thickness as a function of *P*-wave velocity contrast across the LAB beneath the Kaapvaal Craton (red line), Zimbabwe Craton (blue line) and Limpopo Belt (green line).

ness beneath the Zimbabwe Craton and Limpopo Belt is about 215 km and 175 km, respectively, which are also comparable to most of the previous seismic tomographic studies (Li and Burke, 2006; Chevrot and Zhao, 2007). It must be emphasized that the estimated lithospheric thicknesses are under the assumption that there is a sharp boundary between the lithosphere and the asthenosphere, while in reality a gradual rather than sharp transitional zone between the two layers might be present (e.g., Fischer et al., 2010). In this case the estimated depths approximately represent the center of the transitional layer.

## 5. Conclusions

Using an unprecedented number of RFs recorded in southern Africa over the past 27 yr, we imaged the topography of the *d*410 and *d*660 under the non-plane wave assumption. Beneath most of the study area, the *d*410 and *d*660 are apparently shallower than the global average and are parallel to each other, suggesting high wave speed anomalies in the upper mantle. The shallower-than-normal MTZ discontinuities can be sufficiently explained by variations in lithospheric thickness. The resulting MTZ thickness is comparable to the globally averaged value of 250 km, and there is no discernible difference between the on and off cratonic regions. The sharp arrivals associated with both the *d*410 and *d*660 imply the absence of an excessive amount of water in the MTZ, and the lack of a robust negative arrival above the *d*410 is inconsistent with the presence of a water-saturated layer atop the *d*410. The observations suggest that both the cratonic keels and the lower mantle African Superswell have a limited influence on the thermal structure of the mantle transition zone beneath southern Africa.

## Acknowledgements

Data used in this study were requested from the IRIS DMC (last accessed: August 2017). We thank two anonymous reviewers and the editor for suggestions that significantly improved the manuscript. The study was partially supported by the Continental Dynamics Program of the U.S. National Science Foundation under grants No. 1009946 and 1321656 to S.G. and K.L., and by the China Scholarship Council to M.S. under award 201508230075.

## Appendix A. Supplementary material

Supplementary material related to this article can be found online at https://doi.org/10.1016/j.epsl.2018.09.012.

## References

Ammon, C.J., 1991. The isolation of receiver effects from teleseismic P waveforms. Bull. Seismol. Soc. Am. 81, 2504–2510.
Anderson, D.L., 1967. Phase changes in the upper mantle. Science 157, 1165–1173.
Blum, J., Shen, Y., 2004. Thermal, hydrous, and mechanical states of the mantle transition zone beneath southern Africa. Earth Planet. Sci. Lett. 217, 367–378. http://doi.org/10.1016/S0012-821X(03)00628-9.
Chevrot, S., Vinnik, L., Montagner, J.P., 1999. Global-scale analysis of the mantle Pds phases. J. Geophys. Res., Solid Earth 104, 20203–20219. http://doi.org/10.1029/1999JB900087.
Chevrot, S., Zhao, L., 2007. Multiscale finite-frequency Rayleigh wave tomography of the Kaapvaal craton. Geophys. J. Int. 169, 201–215. http://doi.org/10.1111/j.1365-246X.2006.03289.x.
Dahm, H.H., Gao, S.S., Kong, F., Liu, K.H., 2017. Topography of the mantle transition zone discontinuities beneath Alaska and its geodynamic implications: constraints from receiver function stacking. J. Geophys. Res., Solid Earth 122, 10352–10363. http://doi.org/10.1002/2017JB014604.
Dueker, K.G., Sheehan, A.F., 1998. Mantle discontinuity structure beneath the Colorado rocky mountains and high plains. J. Geophys. Res., Solid Earth 103, 7153–7169. http://doi.org/10.1029/97JB03509.
Eaton, D.W., Darbyshire, F., Evans, R.L., Grütter, H., Jones, A.G., Yuan, X., 2009. The elusive lithosphere–asthenosphere boundary (LAB) beneath cratons. Lithos 109, 1–22. http://doi.org/10.1016/j.lithos.2008.05.009.
Efron, B., Tibshirani, R., 1986. Bootstrap methods for standard errors, confidence intervals, and other measures of statistical accuracy. Stat. Sci. 1, 54–75. https://doi.org/10.1214/ss/1177013815.
Fischer, K.M., Ford, H.A., Abt, D.L., Rychert, C.A., 2010. The lithosphere–asthenosphere boundary. Annu. Rev. Earth Planet. Sci. 38, 551–575. https://doi.org/10.1146/annurev-earth-040809-152438.
Fishwick, S., 2010. Surface wave tomography: imaging of the lithosphere–asthenosphere boundary beneath central and southern Africa? Lithos 120, 63–73. http://doi.org/10.1016/j.lithos.2010.05.011.
Flanagan, M.P., Shearer, P.M., 1998. Global mapping of topography on transition zone velocity discontinuities by stacking SS precursors. J. Geophys. Res., Solid Earth 103, 2673–2692. http://doi.org/10.1029/97JB03212.
Foulger, G.R., Panza, G.F., Artemieva, I.M., Bastow, I.D., Cammarano, F., Evans, J.R., Hamilton, W.B., Julian, B.R., Lustrino, M., Thybo, H., Yanovskaya, T.B., 2013. Caveats on tomographic images. Terra Nova 25, 259–281. http://doi.org/10.1111/ter.12041.
Gao, S.S., Liu, K.H., 2014a. Imaging mantle discontinuities using multiply-reflected *P*-to-*S* conversions. Earth Planet. Sci. Lett. 402, 99–106. http://doi.org/10.1016/j.epsl.2013.08.025.
Gao, S.S., Liu, K.H., 2014b. Mantle transition zone discontinuities beneath the contiguous United States. J. Geophys. Res., Solid Earth 119, 6452–6468. http://doi.org/10.1002/2014JB011253.
Gao, S.S., Silver, P.G., Liu, K.H., 2002. Mantle discontinuities beneath southern Africa. Geophys. Res. Lett. 29, 129–1–129-4. http://doi.org/10.1029/2001GL013834.
Gu, Y., Dziewonski, A.M., Agee, C.B., 1998. Global de-correlation of the topography of transition zone discontinuities. Earth Planet. Sci. Lett. 157, 57–67. http://doi.org/10.1016/S0012-821X(98)00027-2.
Hu, J., Liu, L., Faccenda, M., Zhou, Q., Fischer, K.M., Marshak, S., Lundstrom, C., 2018. Modification of the Western Gondwana craton by plume–lithosphere interaction. Nat. Geosci. 11, 203–210. https://doi.org/10.1038/s41561-018-0064-1.
James, D., Fouch, M., VanDecar, J., Van Der Lee, S., 2001. Tectospheric structure beneath southern Africa. Geophys. Res. Lett. 28, 2485–2488. http://doi.org/10.1029/2000GL012578.
Julia, J., Nyblade, A.A., 2013. Probing the upper mantle transition zone under Africa with *P*520*s* conversions: implications for temperature and composition. Earth Planet. Sci. Lett. 368, 151–162. http://doi.org/10.1016/j.epsl.2013.02.021.
Li, A., Burke, K., 2006. Upper mantle structure of southern Africa from Rayleigh wave tomography. J. Geophys. Res., Solid Earth 111, B10303. http://doi.org/10.1029/2006JB004321.
Li, A., Forsyth, D.W., Fischer, K.M., 2003. Shear velocity structure and azimuthal anisotropy beneath eastern North America from Rayleigh wave inversion. J. Geophys. Res., Solid Earth 108, 2362. http://doi.org/10.1029/2002JB002259.
Litasov, K.D., Ohtani, E., Sano, A., Suzuki, A., Funakoshi, K., 2005. Wet subduction versus cold subduction. Geophys. Res. Lett. 32, L13312. http://doi.org/10.1029/2005GL022921.
Lithgow-Bertelloni, C., Silver, P.G., 1998. Dynamic topography, plate driving forces and the African superswell. Nature 395, 269. http://doi.org/10.1038/26212.
Liu, K.H., Gao, S.S., 2010. Spatial variations of crustal characteristics beneath the Hoggar swell, Algeria, revealed by systematic analyses of receiver functions from a single seismic station. Geochem. Geophys. Geosyst. 11, Q08011. http://doi.org/10.1029/2010GC003091.
Liu, K.H., Gao, S.S., Silver, P.G., Zhang, Y., 2003. Mantle layering across central South America. J. Geophys. Res., Solid Earth 108, 2510. http://doi.org/10.1029/2002JB002208.
Liu, L., Gao, S., 2018. Lithospheric layering beneath the contiguous United States constrained by S-to-P receiver functions. Earth Planet. Sci. Lett. 495, 79–86. https://doi.org/10.1016/j.epsl.2018.05.012.

Ni, S., Helmberger, D.V., Tromp, J., 2005. Three-dimensional structure of the African superplume from waveform modeling. Geophys. J. Int. 161, 283–294. http://doi.org/10.1111/j.1365-246X.2005.02508.x.

Niu, F., Levander, A., Cooper, C.M., Lee, C.-T.A., Lenardic, A., James, D.E., 2004. Seismic constraints on the depth and composition of the mantle keel beneath the Kaapvaal craton. Earth Planet. Sci. Lett. 224, 337–346. http://doi.org/10.1016/j.epsl.2004.05.011.

Priestley, K., McKenzie, D., Debayle, E., Pilidou, S., 2008. The African upper mantle and its relationship to tectonics and surface geology. Geophys. J. Int. 175, 1108–1126. http://doi.org/10.1111/j.1365-246X.2008.03951.x.

Reed, C.A., Gao, S.S., Liu, K.H., Yu, Y., 2016. The mantle transition zone beneath the Afar Depression and adjacent regions: implications for mantle plumes and hydration. Geophys. J. Int. 205, 1756–1766. http://doi.org/10.1093/gji/ggw116.

Ringwood, A.E., 1975. Composition and Petrology of the Earth's Mantle, vol. 672, 1st ed. McGraw–Hill, New York.

Ritsema, J., Nyblade, A.A., Owens, T.J., Langston, C.A., VanDecar, J.C., 1998. Upper mantle seismic velocity structure beneath Tanzania, east Africa: implications for the stability of cratonic lithosphere. J. Geophys. Res., Solid Earth 103, 21201–21213. http://doi.org/10.1029/98JB01274.

Ritsema, J., van Heijst, H.J., Woodhouse, J.H., 1999. Complex shear wave velocity structure imaged beneath Africa and Iceland. Science 286, 1925–1928. http://doi.org/10.1126/science.286.5446.1925.

Romanowicz, B., Gung, Y., 2002. Superplumes from the core–mantle boundary to the lithosphere: implications for heat flux. Science 296, 513–516. http://doi.org/10.1126/science.1069404.

Rychert, C.A., Rondenay, S., Fischer, K.M., 2007. *P*-to-*S* and *S*-to-*P* imaging of a sharp lithosphere–asthenosphere boundary beneath eastern North America. J. Geophys. Res., Solid Earth 112, B08314. http://doi.org/10.1029/2006JB004619.

Schaeffer, A.J., Lebedev, S., 2013. Global shear speed structure of the upper mantle and transition zone. Geophys. J. Int. 194, 417–449. https://doi.org/10.1093/gji/ggt095.

Shen, Y., Blum, J., 2003. Seismic evidence for accumulated oceanic crust above the 660-km discontinuity beneath southern Africa. Geophys. Res. Lett. 30, 1925. http://doi.org/10.1029/2003GL017991.

Smyth, J.R., Frost, D.J., 2002. The effect of water on the 410-km discontinuity: an experimental study. Geophys. Res. Lett. 29, 123-1–123-4. http://doi.org/10.1029/2001GL014418.

Sun, M., Liu, K.H., Fu, X., Gao, S.S., 2017. Receiver function imaging of mantle transition zone discontinuities beneath the Tanzania craton and adjacent segments of the east African rift system. Geophys. Res. Lett. 44, 12116–12124. http://doi.org/10.1002/2017GL075485.

Tauzin, B., Debayle, E., Wittlinger, G., 2008. The mantle transition zone as seen by global *Pds* phases: no clear evidence for a thin transition zone beneath hotspots. J. Geophys. Res., Solid Earth 113, B08309. http://doi.org/10.1029/2007JB005364.

Tauzin, B., Debayle, E., Wittlinger, G., 2010. Seismic evidence for a global low-velocity layer within the Earth's upper mantle. Nat. Geosci. 3, 718–721. http://doi.org/10.1038/ngeo969.

Tauzin, B., Ricard, Y., 2014. Seismically deduced thermodynamics phase diagrams for the mantle transition zone. Earth Planet. Sci. Lett. 401, 337–346. http://doi.org/10.1016/j.epsl.2014.05.039.

Thompson, D.A., Helffrich, G., Bastow, I.D., Kendall, J.M., Wookey, J., Eaton, D.W., 2011. Implications of a simple mantle transition zone beneath cratonic North America. Earth Planet. Sci. Lett. 312, 28–36. https://doi.org/10.1016/j.epsl.2011.09.037.

Van der Meijde, M., Marone, F., Giardini, D., Van der Lee, S., 2003. Seismic evidence for water deep in Earth's upper mantle. Science 300, 1556–1558. http://doi.org/10.1126/science.1083636.

Wittlinger, G., Farra, V., 2007. Converted waves reveal a thick and layered tectosphere beneath the Kalahari super-craton. Earth Planet. Sci. Lett. 254, 404–415. http://doi.org/10.1016/j.epsl.2006.11.048.

Wood, B., Pawley, A., Frost, D., 1996. Water and carbon in the Eartha's mantle. Philos. Trans. R. Soc., Math. Phys. Eng. Sci. 354, 1495–1551. http://doi.org/10.1098/rsta.1996.0060.

Youssof, M., Thybo, H., Artemieva, I., Levander, A., 2015. Upper mantle structure beneath southern African cratons from seismic finite-frequency P- and S-body wave tomography. Earth Planet. Sci. Lett. 420, 174–186. http://doi.org/10.1016/j.epsl.2015.01.034.

Yu, Y., Liu, K.H., Moidaki, M., Reed, C.A., Gao, S.S., 2015. No thermal anomalies in the mantle transition zone beneath an incipient continental rift: evidence from the first receiver function study across the Okavango Rift Zone, Botswana. Geophys. J. Int. 202, 1407–1418. http://doi.org/10.1093/gji/ggv229.